



Full Text View

[Volume 30, Issue 9 \(September 2000\)](#)

Journal of Physical Oceanography

Article: pp. 2214–2230 | [Abstract](#) | [PDF \(467K\)](#)

Mesoscale Currents on the Inner New Jersey Shelf Driven by the Interaction of Buoyancy and Wind Forcing

Alexander E. Yankovsky

Graduate College of Marine Studies, University of Delaware, Newark, Delaware, and Nova Southeastern University Oceanographic Center, Dania Beach, Florida

Richard W. Garvine

Graduate College of Marine Studies, University of Delaware, Newark

Andreas Münchow

Institute of Marine and Coastal Sciences, Rutgers University, New Brunswick, New Jersey

(Manuscript received January 25, 1999, in final form October 15, 1999)

DOI: 10.1175/1520-0485(2000)030<2214:MCOTIN>2.0.CO;2

ABSTRACT

Shipboard hydrographic and acoustic Doppler current profiler surveys conducted in August 1996 on the New Jersey inner shelf revealed a buoyant intrusion advancing southward along the coast. This buoyant intrusion originated from the Hudson estuary more than 100 km upshelf and appeared as a bulge of less saline water with a sharp across-shelf frontal zone at its leading edge. During this time, the study area was also forced by a brief upwelling-favorable wind event opposing the direction of buoyant flow propagation.

The interaction of buoyancy and wind forcing generated a spatially variable velocity field. In particular, across-shelf currents were comparable to their alongshelf counterparts. Variability in the alongshelf direction occurred on the scales of the order of the baroclinic Rossby radius. Intensive across-shelf currents reached speeds of 20–40 cm s⁻¹ and appeared as spatially localized mesoscale flows with a width of $O(10)$ km. They were generated at the leading edge of the buoyant intrusion and persisted over the period of observations, slowly propagating southward along with the buoyant flow. They were essentially baroclinic with strong vertical shear and were further amplified by the wind forcing.

The upwelling-favorable wind event also generated cyclonic circulation within

Table of Contents:

- [Introduction](#)
- [Dataset](#)
- [Observations](#)
- [Summary and discussion](#)
- [REFERENCES](#)
- [FIGURES](#)

Options:

- [Create Reference](#)
- [Email this Article](#)
- [Add to MyArchive](#)
- [Search AMS Glossary](#)

Search CrossRef for:

- [Articles Citing This Article](#)

Search Google Scholar for:

- [Alexander E. Yankovsky](#)
- [Richard W. Garvine](#)
- [Andreas Münchow](#)

the buoyant intrusion, which has not been observed before. Interaction of the opposing wind and buoyancy forcings deformed the pycnocline into a dome. This dome was effectively isolated from wind-induced turbulent mixing by overlying buoyant water. The adjustment of the velocity field to this density disturbance occurred geostrophically, even though the water depth was only 20–30 m and friction was important. Relative vorticity associated with this cyclonic flow was at least $0.3f$.

1. Introduction

The great majority of current observations of subtidal frequency shelf circulation depict polarized flow with the across-shelf component much smaller than the alongshelf component. That is, with $\delta = V/U$, where V and U represent the scales for the across-shelf and alongshelf currents, respectively, $\delta \ll 1$. Consistent with this polarization, alongshelf gradients $\partial/\partial x$, are $O(\delta)$ compared to across-shelf gradients $\partial/\partial y$. Advantage is often taken of small δ to simplify theoretical treatments. [Gill and Schumann \(1974\)](#) and [Clarke and Brink \(1985\)](#) have done so in treating fluctuating, low frequency wind-driven shelf flows while [Csanady \(1978\)](#) has used this approximation in developing the arrested topographic wave model.

The observations we report here were of a different character, as they involved a shelf region where δ was $O(1)$ or even greater. Across-shelf currents often exceeded their alongshelf counterparts, while alongshelf gradients were often greater than the across-shelf gradients. The fundamental reason for the unusual properties of the current field was the intrusion of the leading edge of a buoyancy-driven coastal current, the Hudson coastal current, into the study region. Its source was remote, over 100 km upshelf. Adding further surprises to the current structure was the interplay between light wind forcing and the buoyant forcing of the intrusion. As buoyancy sources are common on continental shelves, we expect that our results will have more than merely local implications.

There are numerous observational examples showing the influence of wind forcing on the dynamics of coastal buoyancy-driven currents (or buoyant plumes) at the source region where fresh water is discharged onto the shelf. For instance, [Hickey et al. \(1998\)](#) presented examples of the Columbia River plume response to wind forcing events, including strong winter storms. [Münchow and Garvine \(1993\)](#) studied the effect of upwelling favorable winds on the Delaware plume (Delaware Coastal Current in their terminology). [Boicourt \(1973\)](#) described the dynamics of the Chesapeake plume under different wind conditions; [Bowman \(1978\)](#) reported observations of the Hudson River plume under both upwelling- and downwelling-favorable winds. Interaction of wind- and buoyancy-driven currents has also been studied by numerical modeling: [Chao \(1987, 1988b\)](#), [Kourafalou et al. \(1996\)](#), and [Fong \(1998\)](#).

All these studies show that upwelling favorable wind spreads buoyant water offshore increasing stratification, makes the plume thinner, and in some cases can even separate the plume from the coast. Also, upwelling favorable wind tends to block the natural downshelf (in the direction of Kelvin wave) propagation of the buoyant current. In contrast, a downwelling favorable wind deepens the buoyant plume and makes it narrower, steering buoyant flow along the coast. Downwelling favorable wind greatly facilitates downshelf propagation of the buoyant current.

Buoyant plumes can propagate over a long distance in the downshelf direction and still maintain their structure and strong density contrast with the ambient flow. Upon intruding into a region, the plume strongly modifies the local dynamics and current structure. The dynamics of the leading edge of buoyant plumes and especially the response to wind forcing are poorly understood. [Griffiths and Hopfinger \(1983\)](#) did a laboratory study of the intruding nose of gravity currents with high Reynolds numbers. The propagation speed of the nose was initially that of an internal gravity wave and exponentially decayed with time, while the width of the nose was less than the baroclinic Rossby radius. This flow regime was clearly different compared to our observations. On the other hand, [Chao \(1988a\)](#) showed that at some downshelf distance a buoyant coastal jet widens and forms an anticyclonic geostrophic bulge. [Yankovsky and Garvine \(1998\)](#), hereinafter referred to as YG) presented evidence for the Hudson River plume's arrival off the southern New Jersey coast near Atlantic City. [Münchow and Garvine \(1993\)](#) presented historical observations of the Delaware coastal current which was evident at least 100 km downshelf from its source. [Van der Giessen et al. \(1990\)](#) described the dynamics on the inner Dutch shelf driven by buoyancy and local wind forcing. Buoyant flow originated from the Rhine and Meuse River discharge approximately 50 km upstream. The strongest across-shelf currents were observed in the presence of a strong plume (enhanced discharge), but not always under strong winds. Instead, the wind direction seemed to be more significant. [Rennie et al. \(1999\)](#) reported episodic arrivals of a buoyant intrusion along the North Carolina coast 100 km downshelf from the source, the mouth of the Chesapeake Bay. The timing was controlled by the atmospheric forcing. These papers demonstrate significant downshelf propagation of buoyant flow, but none describes dynamics associated with the advancing leading edge of buoyant intrusion.

In [Fig. 1](#) we show successive maps of the surface salinity field that marked the intrusion of the Hudson coastal current along the extreme southern New Jersey coast in June 1989. Note the very high alongshelf gradients that make up the leading edge of the intrusion. As in the present study, this intrusion was propagating to the south along the coast and then

was nearly 200 km from its source in the Hudson estuary.

In this study we present detailed observations of a similar buoyant intrusion along the New Jersey coast. This intrusion was about 100 km downshelf from the source. During the early part of the observations wind forcing was active and the resulting dynamics was influenced by both wind and buoyancy forcing. The main objective of this paper is to demonstrate that the interaction of a buoyant coastal intrusion with local moderate wind forcing generates vigorous across-shelf currents and alongshelf variability. These results contrast with the common view that across-shelf flows and alongshelf gradients are weak.

These observations are part of a dataset collected in the summer of 1996 on the inner New Jersey shelf off Atlantic City. The main objective of this observational program was to study wind-driven upwelling on the wide, shallow (frictional) shelf. However, the results immediately revealed the strong influence of buoyancy forcing on the local dynamics (YG; [Münchow and Chant 2000](#)).

We summarize the observational dataset and its processing in [section 2](#). The observed current structure is presented in [section 3](#). In total, there were four repeated surveys (“maps”) of the study area. The most significant, map 1, will be described in [section 3a](#), while the most interesting features of the later maps will be presented in [section 3b](#). [Section 4](#) concludes the paper.

2. Dataset

The data presented in this paper comprise current and hydrographic measurements collected from shipboard and moored buoys. Shipboard surveys were conducted by two research vessels from 1 through 6 August 1996. The R/V *Cape Henlopen* completed four repeated maps using the track shown in [Fig. 2](#) (blue circle) from south to north. These observations included acoustic Doppler current profiler (ADCP: a 1228-KHz narrowband) and Scanfish (undulating towed CTD) measurements. The M/V *North Star* surveyed a smaller area covering the nearshore region in the center of the study domain ([Fig. 2](#) (blue circle)). ADCP survey data were averaged over two minute intervals, screened and calibrated according to [Joyce \(1989\)](#). The depth of vertical bins (vertical resolution) was 1 m. CTD (Scanfish) data were screened and averaged over two minute intervals with vertical bins of 0.5 m. Moorings were deployed in water depth ranging from 10 to 25 m along three across-shelf lines ([Fig. 2](#) (blue circle)). InterOcean S4 electromagnetic current meters were deployed at moorings S1, S3, and N1, while bottom mounted RDI ADCPs were placed at C1, C2, C3, and N3 moorings. Further details of the current data obtained from the moorings can be found in [Münchow and Chant \(2000\)](#). We define the coastal coordinate system as follows: the alongshelf coordinate is 60° counterclockwise from true east and the across-shelf coordinate points toward the coast (see [Fig. 2](#) (blue circle)).

We use wind data measured at the Tuckerton Field Station ([Fig. 2](#) (blue circle)) as representative of the local wind forcing. Wind data were obtained from the tower at 9-m height and were averaged hourly. Other available wind time series include data from the environmental buoy EB44009 (Delaware Bay) and from the international airports in Atlantic City and in New York City (JFK). Since the wind speed did not exceed 11 m s^{-1} , we estimated a wind stress using a constant drag coefficient of 1.25×10^{-3} ([Wu 1980](#); YG).

Tidal currents represent one of the major components of the velocity field on the shelf. They would alias shipboard ADCP measurements and thus need to be removed in order to assess nontidal frequency dynamics. In this study, we used the detiding techniques developed by [Münchow \(2000\)](#). The method allows three-dimensional detiding; that is both vertical and horizontal variability of tidal coefficients are resolved by fitting biharmonic splines with the method of least squares ([Sandwell 1987](#)). Münchow tested his tidal prediction for the same study area and found an error of less than 5 cm s^{-1} . His detiding procedure combined both time series from moored buoys and shipboard survey data, but used only the two most significant tidal constituents (a greater number of tidal constituents actually degraded tidal prediction). In this paper we concentrate on the dynamics for water depths from 15 to 30 m and apply a customized version of the [Münchow \(2000\)](#) detiding procedure based on mooring data solely. This method does not resolve all the spatial details of the tidal flow field nearshore (depths less than 10 m) but does allow us to use four tidal constituents (K_1 , O_1 , M_2 , N_2) and so gives better estimation for the tidal parameters offshore. Time series of currents from moorings are detided using harmonic analysis for five tidal constituents.

Tidal prediction was made using the full length of the current time series, almost three months. However, actual currents at the tidal frequencies during any particular period of time could depart from this long-term “harmonic” approximation for a number of reasons, for example, due to nonlinear interaction or generation of baroclinic tides. As a test for this possibility, we also estimated the tidal flow field using just the 7-day time series covering the period of the maps. The resulting prediction of tidal currents was almost identical to the results derived from the full time series (within $1\text{--}2 \text{ cm s}^{-1}$). Thus, we conclude that the tidal regime during the period of observations did not contain significant transient features and was close to its long-term harmonic approximation. [Chant and Münchow \(2000\)](#) showed that inertial currents were weak during this period.

3. Observations

[Figure 3](#) characterizes the forcing agents during the period of observations. The alongshelf and across-shelf components of the local wind stress (Tuckerton station) are shown in [Fig. 3a](#). The most significant wind event occurred on 1 August (before and at the beginning of map 1) with a subsequent, short wind event late on 2 August. Only very light winds were observed later (3–6 August). All available wind records are consistent and show that the winds were upwelling-favorable at all sites of wind observations on 1–2 August. The strongest wind speed was registered at Delaware buoy and Tuckerton station ($10\text{--}11\text{ m s}^{-1}$) while only $5\text{--}6\text{ m s}^{-1}$ at both airports. After this strongest event on 1 August, the wind subsided with typical speeds of $4\text{--}6\text{ m s}^{-1}$.

Throughout the period of observations, buoyant water gradually intruded from north to south. [Figures 3b–d](#) show consecutive plots of surface salinity corresponding to map 1, map 2, and map 4. Initially buoyant water was present only at the northern edge of the study area, while by the end of the observations it occupied both northern and central parts. Buoyant water extended well offshore (25–30 km), a likely consequence of the prevailing upwelling favorable winds in late July (YG). The contrast in salinity between ambient water (slightly higher than 30.5 psu) and buoyant water (28.5 psu in the core of the plume) was weaker than during June and July, associated with the lower discharge of the Hudson River (YG).

Two forcings (wind and buoyancy) opposed each other: upwelling-favorable wind acted northward (upshelf) while the buoyant intrusion propagated southward (downshelf). Wind forcing had a large spatial scale, while buoyancy forcing was confined to the plume.

We will split the description of observations into two parts. We will begin with the description of map 1 when both wind and buoyancy forcing were present. Then we will show subsequent maps to display the temporal evolution of the flow fields. We will not present data from map 3 as it only represented a smooth transition between maps 2 and 4.

a. Map 1: 1–2 August

Sampling for map 1 was conducted from 2305 UTC 1 August through 2050 2 August. The detided velocity field ([Fig. 4](#)) reveals very high alongshelf gradients and large across-shelf currents. Indeed, the across-shelf component was comparable to the alongshelf component, that is, $\delta = O(1)$. We initially interpreted this field as resulting from a malfunction of the shipboard ADCP. However, careful comparison of the ADCP data with other available current measurements taken simultaneously proved their good quality.

Despite the high horizontal gradients, the current field during map 1 had vertical coherence. The currents shown in [Fig. 4a](#) were centered at 4.5-m depth within the upper mixed layer (UML). [Figure 4b](#) shows currents at 9.5-m depth, which is approximately at the bottom of the UML (although the UML depth exhibited substantial variations within the study area). The currents at 4.5 and 9.5 m were similar and generally lacked significant vertical shear. The only exception occurred near the coast where currents at 9.5 m are within the bottom boundary layer. At 14.5 m the currents decreased ([Fig. 4c](#)) and veered counterclockwise.



These highly variable currents suggest that the temporal variability of the flow over a period of observations could be significant and caused some temporal aliasing. However, there were also spatial features in the flow field, which will be described next and which can be determined based on the comparison with other available current data.


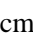




In order to distinguish these spatial structures, we will compare the currents from shipboard ADCP data with those at the moorings. The results are shown in [Fig. 5](#) (alongshelf component) and [Fig. 6](#) (across-shelf component). We chose the ADCP bin centered at 9.5-m depth because it is the uppermost level where the current data are available from all three offshore moorings: S3, C3, and N3 ([Fig. 2](#)). The shipboard detided currents of map 1 are plotted against time as a pseudo time series; ship track waypoints (wp) are also shown on the plot corresponding to times when the ship occupied those positions.



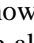
The foundation of our case is the very good agreement between the current data at the moorings and those from the ADCP measured near the mooring locations. Early on 2 August (0000 UTC) the upshelf flow at mooring S3 exceeded 20 cm s^{-1} ([Fig. 5](#), bottom). This upshelf current was also registered by the shipboard ADCP in the vicinity of mooring S3 ([Fig. 5](#), middle). At the same time the alongshelf current at mooring C3 (central location) was zero while at mooring N3 (northern location) it was downshelf ($5\text{--}7\text{ cm s}^{-1}$). Thus, there was a strong convergence (approximately 25 cm s^{-1}) in alongshelf velocity between southern and northern parts of the study area. This convergence was recorded in the shipboard ADCP currents, as well. The ADCP upshelf current quickly decreased as the ship advanced toward the coast (wp B) and then upshelf (wp C, D: [Fig. 5](#), middle). On transect CD (approximately 0430–0630), the upshelf velocity component was only $3\text{--}5\text{ cm s}^{-1}$. At the same time the upshelf flow at mooring S3 remained 20 cm s^{-1} while at C3 it was downshelf with

increasing velocity from 10 to almost 20 cm s⁻¹. As a result, convergence between southern and central moorings remained strong. Farther north, the alongshelf velocity component was negative (directed downshelf) in the second half of 2 August both according to shipboard ADCP and N3 mooring data.



The mooring data also show some temporal variability, not surprising because of the transient wind event. We calculated the lagged cross-correlation coefficients between alongshelf wind stress at Tuckerton and detided alongshelf current component at the S3 and N3 moorings for the two-day records from 0000 1 August through 0000 UTC 3 August when the wind forcing occurred. The maximum cross-correlation coefficient at S3 was 0.996 while at N3 it was 0.857; time lag was between 9 and 10 h. Clearly, the alongshelf current temporal fluctuations were driven by the local wind forcing.


Nevertheless, the direction of the mean current at the northern location (N3 in [Fig. 5](#) , bottom) was opposite to the wind forcing. The opposition is readily explained by the intrusion of buoyant water that is evident in the surface salinity field ([Fig. 4a](#) ). The intruding water was the leading edge of the Hudson coastal current.

The across-shelf currents revealed by the ADCP data are highly variable alongshelf. Yet, where this component could be checked against mooring data, agreement resulted. As the ship passed mooring S3 early on 2 August, the across-shelf currents recorded by both the ADCP and at the mooring were weak ([Fig. 6](#) ). As the ship passed mooring C3 near wp F ten hours later, the flow was onshore at about 10 cm s⁻¹. Between these positions the ADCP recorded coherent offshore flow along CD and DE with speeds up to 40 cm s⁻¹ ([Fig. 6](#) , middle). This flow was not related to temporal variability. Indeed, both S3 and C3 current data show that temporal variations of the across-shelf currents from 0430 to 0830 (time interval of the measurements along the CD and DE lines) were within the range of 10–15 cm s⁻¹ ([Fig. 6](#) , bottom). Accordingly, we interpret this strong offshore flow as a spatial feature. The offshore flow occurred at the same location where the alongshelf component was close to zero (i.e., it changed sign from upshelf to downshelf)—compare [Figs. 5](#)  and [6](#) . We conclude that this strong and spatially localized offshore flow was driven by the convergence of the upshelf wind-driven flow from the south and the downshelf buoyancy-driven flow from the north, which are evident in [Fig. 5](#) .

Farther upshelf, along FG and GH, the ADCP recorded coherent onshore flow with speeds up to 20 cm s⁻¹. The maximum onshore current occurred along the leading edge of the buoyant intrusion from the north (transect GH). Corroboration of this onshore flow along transects FG and GH is obtained from the simultaneous detided Ocean Surface Current Radar (OSCR) system data available for the northern part of the study domain. The OSCR data showed consistently good agreement with the ADCP measurements through the period of observations ([Chant and Münchow 2000](#)). We present these detided OSCR data for two times on 2 August, 1996: at 1000 ([Fig. 7a](#) ) when the ship was approaching wp F along transect EF and at 1700 ([Fig. 7b](#) ) when the ship was in the middle of transect IJ. This is the time interval when onshore flow was observed in the shipboard ADCP data. The detided OSCR data ([Fig. 7](#) ) clearly show a corresponding onshore flow pattern in the surface currents for both snapshots even though the temporal changes were also essential. The width of this flow feature slightly exceeded 10 km.

Currents along transect JK were highly variable. The across-shelf component was toward the coast nearshore while toward the ocean some distance offshore. The spatial location of maximum offshore velocity changed in time over the period of shipboard measurements (1800–2100) according to OSCR data (not shown). This explains some discrepancy between the shipboard ADCP and the N3 mooring data (the former are instantaneous while the latter are averaged over 1 hour).

Thus, while there were essential temporal variations (evident in the mooring and OSCR data), persistent horizontal structure of the currents in the upper layer was present: upshelf and offshore flow in the southern part of the study domain, downshelf and onshore flow in the central part, and downshelf and offshore flow in the northern part. The strongest across-shelf currents tended to be spatially localized with an alongshelf scale $O(10\text{ km})$. The horizontal resolution of the moorings was insufficient to reveal these enhanced flows. However, mooring data were consistent with the shipboard ADCP data measured near the mooring locations. Across-shelf currents strongly depended on the distance from the coast with the lowest values observed at the coastal waypoints ([Figs. 4a](#)  and [6](#) .

The enhanced across-shelf flows that we observed also exhibited strong vertical shear (cf. [Figs. 4b and 4c](#) ). Our study area represents the dynamically complicated inner shelf region where near-geostrophic motions interact with surface and bottom friction layers. Accordingly, there are two sources for the vertical shear of the horizontal velocity: (i) surface or bottom stresses and turbulent friction and (ii) horizontal baroclinic pressure gradient. On the inner shelf, friction layers merge and the friction effects produce a continuous change of the velocity vector in the vertical on the scale of the water depth. Under the observed conditions the stratification could reduce the turbulent friction coefficient in the pycnocline. However, the resulting velocity shear still should be almost uniform through the whole water column. This feature was illustrated by [Lentz \(1995\)](#) in his example of the exponential viscosity profile with close to zero value in the middle of water column. On the other hand, the water in the study area was seasonally stratified with a clear two-layer structure, a thin and very intense pycnocline separating surface and bottom mixed layers. The only exception occurred nearshore at wp J where

the downwelling regime prevailed with the continuous stratification. Thus, we expect that the baroclinic shear for most of the domain would have a local maximum in the vertical within the pycnocline while the frictional shear would be almost uniform.

We analyzed the horizontal distribution of the *mean* vertical shear (averaged over the whole water column) and the *maximum* vertical shear measured by shipboard ADCP during map 1. The mean vertical shear varied between 0.025 and 0.04 s⁻¹ and did not show substantial horizontal changes, while the maximum vertical shear had greater range of horizontal variability with several spatial maxima: in the vicinity of wp C–E (0.15–0.20 s⁻¹), wp G (>0.15 s⁻¹), and in the middle of transect JK (>0.15 s⁻¹). In order to assess the relative importance of the baroclinic vertical shear, we present the horizontal distribution of the *maximum vertical shear* normalized by the local *mean vertical shear* (Fig. 8). For the areas with high values of this normalized maximum shear (say, greater than 4) baroclinic vertical shear prevails while for the areas with the lower numbers (2–3) frictional shear is more significant. In Fig. 8, we plotted only contours 4 and higher in order to emphasize the flows with baroclinic shear. There are two absolute maxima of the normalized shear: one is in the vicinity of wp C (>7) and the other at wp G (>6). These are also the two locations of maximum detided across-shelf velocities: offshore at wp C (almost 40 cm s⁻¹) and onshore at wp G (about 25 cm s⁻¹)—see Figs. 4a,b and Fig. 6.

In the description of the velocity field we pointed out upshelf flow in the southern part and downshelf flow in the northern part. The vertical density structure along transects AB (southern part) and IJ (northern part) demonstrate essentially different dynamical regimes (Fig. 9). In the southern part of the study area the wind stress generated upshelf flow and established an upwelling regime with the pycnocline reaching the surface at the coast on transect AB. Along transect IJ isopycnals instead tilted toward the bottom near the coast. Buoyant water (density less than 1021 kg m⁻³) remained in contact with the bottom near the coast. Thus, the duration and strength of the transient upwelling-favorable wind event was insufficient to detach the advancing buoyant intrusion from the coast and to reverse the buoyancy-driven southward flow.

In Fig. 9 we also plot the vertical distribution of the Richardson number Ri:

$$Ri = -\frac{g}{\rho} \frac{\rho_z}{u_z^2 + v_z^2}, \quad (1)$$

where ρ is the water density, u and v are the horizontal velocity components, g is the gravitational acceleration; subscript z denotes partial differentiation in the vertical (with positive direction upward). We estimated Ri for every vertical bin except those closest to the surface and bottom. We applied central differences to approximate vertical derivatives; thus, each Ri value was estimated over a 2-m depth interval. The minimum Ri value contoured in this plot is 10, because values below 10 turn out to represent the background level. High values (Ri > 10) imply the effective limit for penetration of turbulent mixing caused by the vertical shear of velocity.

Transect AB had the typical vertical structure for upwelling: the pycnocline approached the surface at the coast, both surface and bottom mixed layers were well pronounced, and high values of Ri were observed within the thin, intense pycnocline. Transect IJ had different features: at the coast the isopycnals tilted down toward the bottom and did not form a sharp, thin pycnocline. Instead, the density changed from the surface to the bottom rather gradually. These features are typical for a buoyancy driven coastal current or downwelling regime, when lighter water is driven offshore in the bottom boundary layer, thus mixing with the overlying water and reducing the stratification (Chapman and Lentz 1994). Within 10 km of the coast there were few high values of Ri, implying significant vertical mixing. Farther offshore along transect IJ, the pycnocline structure corresponded to upwelling-favorable wind forcing. Indeed, Fig. 4a shows offshore flow of the surface currents along transects IJ and JK some distance offshore. As a result, the pycnocline was deformed into a domelike shape. The dome was induced by the UML divergence caused, in turn, by the joint action of wind-driven offshore Ekman transport near the surface and the buoyancy-driven nearshore downwelling regime. This latter one drove offshore flow at the bottom with compensating onshore flow at the surface. The center of the dome was at longitude 74.12°W (Fig. 9, lower panel). This dome was not exposed to wind-induced mixing. Instead, the lighter, buoyant water was driven offshore above the “main” pycnocline (associated with the seasonal thermocline, isopycnals 1022–1024). Note the high values of Ri on the top of this dome (Fig. 9).

The baroclinic Rossby radius (R_l) is an appropriate across-shelf scale for baroclinic motions trapped near the coast. For a two-layer approximation, R_l is

$$R_l = \sqrt{\frac{g' h_1 h_2}{f(h_1 + h_2)}}, \quad (2)$$

where h_1 and h_2 are the thicknesses of the surface and bottom layers, f is the Coriolis parameter and g' is the reduced

gravity of the internal interface, $g' = g\Delta\rho/\rho_0$, $\Delta\rho$ is the density difference between the layers, and ρ_0 is the reference density.

Taking the total depth to be 20–25 m with interface in the middle of the water column, $\Delta\rho = 3\text{--}4\text{ kg m}^{-3}$ with the reference density 1022 kg m^{-3} and $f = 0.92 \times 10^{-4}\text{ s}^{-1}$, the estimation for R_i is 4.2–5.4 km. From the velocity field shown in [Fig. 4a](#), the baroclinic Rossby radius seems to be an appropriate scale for the *alongshelf* adjustment of the observed mesoscale flows.

b. Maps 2 and 4: 3–6 August

After map 1 was completed, the wind slackened so that map 2 was conducted under conditions of light wind forcing from 0304 3 August through 0300 4 August ([Fig. 3](#)). [Figure 10](#) shows the detided velocity field in the UML derived from the ADCP shipboard measurements. Compared to the previous map the currents were weaker except in the northern part of the domain where the buoyant intrusion was advancing. The across-shelf component of the flow field is reminiscent of the previous map with offshore flow within the advancing edge of the buoyant intrusion, onshore flow in the central part (transect EF), and offshore flow in the southern part (wps A, C) of the study domain. These flow features moved southward relative to map 1 but they retained their position relative to the advancing buoyant intrusion. Indeed, the surface salinity distributions indicate that the intrusion in the northern part was gradually moving downshelf (cf. [Figs. 4a](#) and [10](#)). At this time the leading edge reached transect FG. As a result, the system of mesoscale currents associated with this plume also moved downshelf.

The most unusual and interesting feature of the velocity field is the cyclonic circulation within the buoyant intrusion. Most theoretical and modeling studies predict an anticyclonic regime of circulation around the bulge of buoyant water near the plume source: [Garvine \(1987\)](#), [Chao \(1988a\)](#), [Yankovsky and Chapman \(1997\)](#). However, all these papers deal with plumes unforced by wind.

The vertical transect of detided alongshelf velocity and density along JK is presented in [Fig. 11a](#). The density field was averaged (“soothed”) in order to remove smaller scale features, which are typically associated with internal waves. These features are evident, for example, in [Fig. 9](#) and can degrade the estimation of the geostrophic velocity component. The isopycnal surfaces are dome shaped. The formation of this dome structure was evident earlier, during map 1 ([Fig. 9](#)); now the dome’s center extended seaward to longitude 74.0°W . Moreover, both positive (upshelf) and negative (downshelf) velocities are consistent with this density structure in the manner of geostrophic adjustment. Maximum velocity and vertical shear occurred precisely where the maximum horizontal density gradient was observed, that is, on both sides of the dome ([Fig. 11a](#)). The alongshelf velocity shear was approximately 60 cm s^{-1} over 22 km. Thus, relative vorticity of this cyclonic feature is about $0.3f$, where f is the planetary vorticity.

We estimated the geostrophic vertical shear of the alongshelf current based on thermal wind balance ([Gill 1982](#)) and show the results in [Fig. 11b](#). As a reference level, we used the observed alongshelf velocity at 6.5-m depth and calculated the geostrophic velocity downward. The geostrophic velocity gives good *qualitative* agreement with the observed velocity. Moreover, even absolute values of the geostrophic shear are close to those observed. The only exception occurs at 73.9°W where the geostrophic vertical shear substantially overestimates the observed. Here a very intense pycnocline (3 kg m^{-3} over 5 m in vertical) leads to unrealistically high thermal wind shear. The important feature is that the actual velocity shear nearshore (depth 15–20 m, where the downwelling regime exists) is in good agreement with the geostrophic estimation, showing no indication of bottom stress influence. This resembles the dynamics of the slippery boundary layer ([Garrett et al. 1993](#); [Chapman and Lentz 1997](#)), when the combination of density gradient and sloping bottom significantly reduces the bottom stress.

The dome of the pycnocline was formed due to divergence in the surface Ekman layer associated with the competition between two opposing forcings: wind and buoyancy. The upwelling-favorable wind produced offshore Ekman transport in the surface boundary layer while buoyancy forcing still maintained a downwelling regime near the coast ([Fig. 9](#)). This downwelling circulation consisted of offshore transport in the bottom boundary layer with compensating onshore flow at the surface. The divergence in the surface Ekman layer caused the rise of the pycnocline at this location. The divergence point can be seen in [Fig. 4a](#) on transect JK (approximately halfway between wp J and mooring N3). The geostrophic adjustment of the flow field to this density structure resulted in the observed cyclonic current within the intrusion. Even though this cyclonic feature was formed on the inner shelf where turbulent friction dominates, it seems to be a robust feature. This dome was shielded from erosion by wind-induced mixing by the buoyant water on top of it that was spread offshore by the upwelling-favorable wind. At the same time, the actual alongshelf velocity at the bottom ([Fig. 11a](#)) was close to zero due to strong vertical shear. This cyclonic flow, thus, was not exposed to strong bottom friction.

The velocity field observed during map 3 (4–5 August) was qualitatively similar to map 2. The buoyant intrusion advanced farther downshelf and the cyclonic circulation within it persisted. The final map, map 4, was conducted from 0630 5 August through 0335 6 August. During the second half of this map, the upwelling-favorable wind slightly increased ([Fig. 3](#)), which could have amplified cyclonic flow within the intrusion. As in the two previous maps, cyclonic flow remained the

most prominent feature of the velocity field in the UML (Fig. 12). Below the pycnocline (15 m and deeper) this feature could hardly be seen, revealing the essentially baroclinic nature of this cyclonic flow. By this time, the buoyant intrusion had advanced to transect DE (Fig. 12). The offshore extension of the intrusion did not change from that of map 2 due to the lack of upwelling favorable winds between 3 and 5 August (Fig. 3). There is good agreement between the cyclonic pattern of UML currents and the configuration of the intrusion. Moreover, there is evidence of cyclonic circulation in the surface salinity distribution: a tongue of fresher water detached from the coast and turned offshore near wp F (Fig. 12). At wp E the current flowed toward the coast and then turned in the downshelf direction along transect DE. This might be evidence of the *anticyclonic* flow surrounding the bulge of buoyant water, as suggested by numerous theoretical and modeling studies.

The vertical structure of the density field reflected the different dynamical regimes in the northern, central and southern parts of the study area. Along transect AB, the “standard” water structure was observed: a flat and sharp pycnocline at the depth of 10–15 m separated surface and bottom mixed layers (Fig. 13a). Along transect EF flow convergence was evident in the across-shelf velocity component (Fig. 12) that resulted in continuously stratified water structure from surface to bottom (Fig. 13b). Finally, isopycnals on transect IJ (Fig. 13c) again revealed the dome structure associated with cyclonic flow within the plume. Over the top of this dome there was a thin layer of fresher buoyant water. These three very different across-shelf density sections well illustrate the striking alongshelf variability. The three sections of Fig. 13 are separated alongshelf by only about 20 km.

4. Summary and discussion

This paper presents the observations of a buoyant intrusion advancing along the southern New Jersey coast that originated from the Hudson estuary more than 100 km upshelf. This buoyant intrusion appeared as a bulge of less saline water with a rather sharp frontal zone at its leading edge that ran almost perpendicular to the coastline. The arrival of buoyant water set up strong density gradients in the alongshelf direction. The study area was also forced by a brief upwelling-favorable wind event opposing the direction of buoyant flow propagation. The interaction of buoyancy and wind forcing generated a velocity field with large horizontal variability on the inner shelf in water depths of 10–30 m. These mesoscale currents varied in the *alongshelf* direction on spatial scales of the order of the baroclinic Rossby radius. Vorticity associated with the observed currents was at least $0.3f$. Probably the most remarkable feature of the observed fields is the intensive across-shelf currents with velocities in the range of 20–40 cm s^{-1} . These across-shelf currents were baroclinic, with strong vertical shear. They were concentrated at the edges of buoyant flow. However, the wind forcing further amplified them. According to our observations, the width of such across-shelf currents is $O(10 \text{ km})$ or of the order of the baroclinic Rossby radius.

Other observations on inner shelves, including the California coast (Lentz 1994) and the Scotian shelf (Schwing 1992), did not reveal similar enhanced across-shelf currents or their alongshelf variability. The likely reason is that the inner-shelf flow in those cases had almost uniform density. Nevertheless, it is difficult to detect such flow features, especially if one uses only low-pass filtered time series obtained from a sparse array of moorings. Indeed, these features have compact alongshelf and across-shelf spatial structures and propagate in the alongshelf direction with the buoyant intrusion. Thus, they can appear as high-frequency fluctuations in the Eulerian sense, that is, at a fixed location and so can be obscured by low-pass filtering. “Conventional” analysis of the subinertial dynamics in this area based on low-pass filtered current time series from moorings did not show unusual mesoscale variability during this period of time (YG).

The observed forcing conditions during our study were typical for the summer season along the U.S. East Coast. There are numerous sources of buoyancy there and upwelling-favorable winds prevail. Thus, the observed fields should be typical rather than anomalous phenomena providing significant across-shelf exchange on the inner shelf in the vicinity of a buoyant intrusion.

Another interesting feature of the observations is the formation of cyclonic circulation within the buoyant intrusion. This has not been observed or predicted theoretically before. This feature was likely caused by the interaction of buoyancy and wind forcing. The buoyant intrusion propagated downshelf with corresponding downwelling circulation near the coast and with offshore transport in the bottom Ekman layer, as in the model of Chapman and Lentz (1994). However, the upwelling-favorable wind drove offshore flow in the surface Ekman layer and generated an upwelling regime outside the buoyant intrusion. The wind event was not strong enough or long enough to transport all buoyant water offshore and completely detach the buoyant intrusion from the coast. Instead, the pycnocline was deformed into a dome. This dome was effectively isolated from wind-induced turbulent mixing by the overlying buoyant water. The evolution of the velocity field occurred in the manner of geostrophic adjustment, even though the total water depth was only 15–30 m and friction was important.

Indeed, observed alongshelf velocity and the estimated geostrophic component through the across-shelf section (Fig. 11) were in good qualitative agreement. More remarkably, estimated (geostrophic) and actual vertical shears were also similar on the inner shelf except where the pycnocline was locally intense. The geostrophic component of the inner-shelf velocity field seems to be a robust feature in this regime of strong stratification. This was also a feature of the numerical simulations of both upwelling dynamics by Allen et al. (1995) and buoyancy-driven currents by Chapman and Lentz (1994).

The cartoon shown in [Fig. 14](#) generalizes the observations. Since the prevailing wind along the New Jersey coast is upwelling-favorable in summer, buoyant plumes originating from the Hudson River discharge can propagate downshelf only episodically when the wind is weak or changes direction (YG). Buoyant intrusions tend to arrive off the southern New Jersey coast as individual features, not as a continuous and persistent buoyant current along the whole New Jersey coast ([Münchow 1992](#)). In our case, the arriving intrusion was affected by the moderate wind forcing events. As a result, cyclonic circulation developed within the intrusion while weaker anticyclonic flow surrounded it. The anticyclonic regime was especially evident during map 1 at the leading edge of the intrusion. Slightly downshelf, an upwelling regime was established with strong offshore flow.

This depiction in [Fig. 14](#) is highly idealized; the observed velocity field exhibited essential temporal variability. Yet these features were repeatedly observed during subsequent maps while the whole system gradually propagated downshelf along with the buoyant water.

Acknowledgments

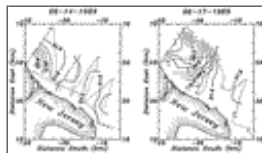
This was a joint project between Rutgers University and the University of Delaware supported by Grants OCE-9521102 at Delaware and OCE-9528239 at Rutgers from the U.S. National Science Foundation. AY was supported by the NSF Grant OCE-9730026. We thank Scott Glenn for providing the Tuckerton tower data. Robert Chant, Todd Sanders, and Pablo Clemente-Colon supported the shipboard data collection, while Timothy Pfeiffer provided support service as oceanographic technician.

REFERENCES

- Allen, J. S., P. A. Newberger, and J. Federiuk, 1995: Upwelling circulation on the Oregon continental shelf. Part I. Response to idealized forcing. *J. Phys. Oceanogr.*, **25**, 1843–1866.
- Boicourt, W. C., 1973: The circulation of water on the continental shelf from Chesapeake Bay to Cape Hatteras. Ph.D. dissertation, The Johns Hopkins University, 183 pp.
- Bowman, M. J., 1978: Spreading and mixing of the Hudson River effluent into the New York Bight. *Hydrodyn. Est. Fjords.*, **23**, 373–386.
- Chant, R. J., and A. Münchow, 2000: Evolution of near inertial waves during an upwelling event on the New Jersey inner shelf. *J. Phys. Oceanogr.*, in press.
- Chao, S.-Y., 1987: Wind-driven motion near inner shelf fronts. *J. Geophys. Res.*, **92**, 3849–3860.
- , 1988a: River-forced estuarine plumes. *J. Phys. Oceanogr.*, **18**, 72–88.
- , 1988b: Wind-driven motion of estuarine plumes. *J. Phys. Oceanogr.*, **18**, 1144–1166.
- Chapman, D. C., and S. J. Lentz, 1994: Trapping of a coastal density front by the bottom boundary layer. *J. Phys. Oceanogr.*, **24**, 1464–1479.
- , and —, 1997: Adjustment of stratified flow over a sloping bottom. *J. Phys. Oceanogr.*, **27**, 340–356.
- Clarke, A. J., and K. H. Brink, 1985: The response of stratified, frictional flow of shelf and slope waters to fluctuating large scale, low-frequency wind forcing. *J. Phys. Oceanogr.*, **15**, 439–453.
- Csanady, G. T., 1978: The arrested topographic wave. *J. Phys. Oceanogr.*, **8**, 47–62.
- Fong, D. A., 1998: Dynamics of freshwater plumes. Ph.D. thesis, MIT/WHOI Joint Program in Oceanography, 155 pp.
- Garrett, C., P. MacCready, and P. Rhines, 1993: Boundary mixing and arrested Ekman layers: rotating stratified flow near a sloping boundary. *Annu. Rev. Fluid Mech.*, **25**, 291–323.
- Garvine, R. W., 1987: Estuary plumes and fronts in shelf waters: a layer model. *J. Phys. Oceanogr.*, **17**, 1877–1896.
- Gill, A. E., 1982: *Atmosphere–Ocean Dynamics*. Academic Press, 662 pp.
- , and E. H. Schumann, 1974: The generation of long shelf waves by the wind. *J. Phys. Oceanogr.*, **4**, 83–90.
- Griffiths, R. W., and E. J. Hopfinger, 1983: Gravity currents moving along a lateral boundary in a rotating fluid. *J. Fluid Mech.*, **134**, 357–

- Hickey, B. M., L. J. Pietrafesa, D. A. Jay, and W. C. Boicourt, 1998: The Columbia River plume study: Subtidal variability in the velocity and salinity fields. *J. Geophys. Res.*, **103**, 10339–10368.
- Joyce, T. M., 1989: On in situ “calibration” of shipboard ADCPs. *J. Atmos. Oceanic Technol.*, **6**, 169–172.
- Kourafalou, V. H., L.-Y. Oey, J. D. Wang, and T. N. Lee, 1996: The fate of river discharge on the continental shelf. 1. Modeling the river plume and the inner shelf coastal current. *J. Geophys. Res.*, **101**, 3415–3434.
- Lentz, S. J., 1994: Current dynamics over the northern California inner shelf. *J. Phys. Oceanogr.*, **24**, 2461–2478.
- , 1995: Sensitivity of the inner-shelf circulation to the form of the eddy viscosity profile. *J. Phys. Oceanogr.*, **25**, 19–28.
- Münchow, A., 1992: The formation of a buoyancy driven coastal current. Ph.D. dissertation, University of Delaware, 205 pp.
- , 2000: Detiding three-dimensional velocity survey data in coastal waters. *J. Atmos. Oceanic Technol.*, **17**, 736–749.
- , and R. W. Garvine, 1993: Buoyancy and wind forcing of a coastal current. *J. Mar. Res.*, **51**, 293–322.
- , and R. J. Chant, 2000: Kinematics of inner shelf motions during the summer stratified season off New Jersey. *J. Phys. Oceanogr.*, **30**, 247–268.
- Rennie, S. E., J. L. Largier, and S. J. Lentz, 1999: Observations of a pulsed buoyancy current downstream of Chesapeake Bay. *J. Geophys. Res.*, **104**, 18227–18240.
- Sandwell, D. T., 1987: Biharmonic spline interpolation in GEOS-3 and SEASAT altimeter data. *Geophys. Res. Lett.*, **23**, 2101–2104.
- Schwing, F. B., 1992: Subtidal response of Scotian Shelf circulation to local and remote forcing. Part I: Observations. *J. Phys. Oceanogr.*, **22**, 523–541.
- Van der Giessen, A., W. P. M. de Ruijter, and J. C. Borst, 1990: Three-dimensional current structure in the Dutch coastal zone. *Neth. J. Sea Res.*, **25** (1/2), 45–55.
- Wu, J., 1980: Wind-stress coefficients over sea surface near neutral conditions—A revisit. *J. Phys. Oceanogr.*, **10**, 727–740.
- Yankovsky, A. E., and D. C. Chapman, 1997: A simple theory for the fate of buoyant coastal discharges. *J. Phys. Oceanogr.*, **27**, 1386–1401.
- , and R. W. Garvine, 1998: Subinertial dynamics on the inner New Jersey shelf during the upwelling season. *J. Phys. Oceanogr.*, **28**, 2444–2458.

Figures



[Click on thumbnail for full-sized image.](#)

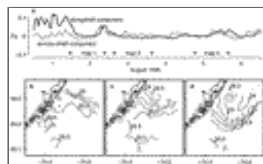
Fig. 1. Map of surface salinity showing the downshelf progress of the leading edge of the Hudson Coastal Current off the southern New Jersey coast. Cape May is at the lower right. Dotted lines denote the ship track (from [Münchow 1992](#)). Left panel: map of 14 Jun 1989; right panel: map of 17 Jun 1989



[Click on thumbnail for full-sized image.](#)

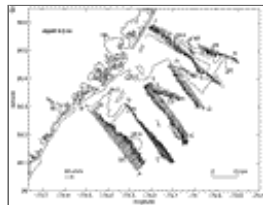
Fig. 2. Map of the study area off the New Jersey coast showing the positions of moorings (asterisks), wind observations (solid

circle), and ship track (dashed line)



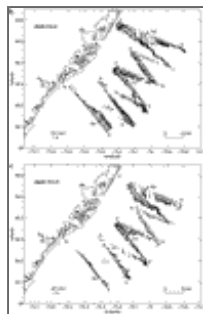
[Click on thumbnail for full-sized image.](#)

Fig. 3. (a) Wind stress time series measured at the Tuckerton Station: heavy/light line is alongshelf/across-shelf component. Positive values denote upshelf/onshore direction. Time intervals of the hydrographic surveys are shown with asterisks. Surface salinity measured during (b) map 1, (c) map 2, and (d) map 4



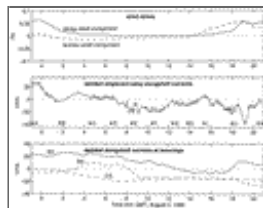
[Click on thumbnail for full-sized image.](#)

Fig. 4. Map 1 detided shipboard ADCP velocity field at (a) 4.5-m depth, (b) 9.5-m depth, and (c) 14.5-m depth. Asterisks show mooring locations. Surface salinity distribution is shown in (a)



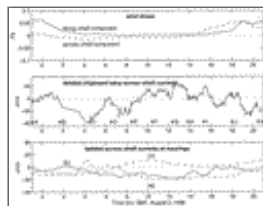
[Click on thumbnail for full-sized image.](#)

Fig. 4. (Continued)



[Click on thumbnail for full-sized image.](#)

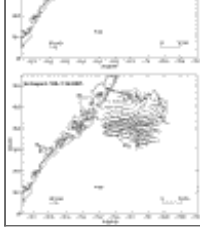
Fig. 5. Time series of wind stress components at the Tuckerton Station (top); detided shipboard ADCP alongshelf velocity component at 9.5-m depth (middle). (Asterisks show waypoints during map 1); detided alongshelf velocity component measured at the moorings (bottom) S3 (solid line) at 9-m depth, C3 (dash-dotted line) at 9.5-m depth, and N3 (dashed line) at 9.2-m depth. Positive values denote the upshelf direction



[Click on thumbnail for full-sized image.](#)

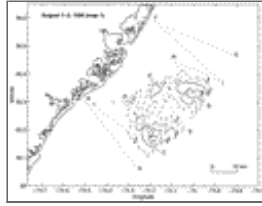
Fig. 6. As in [Fig. 5](#) but for the across-shelf component. Positive values denote the onshore direction





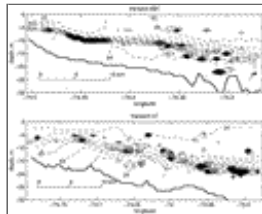
[Click on thumbnail for full-sized image.](#)

Fig. 7. Detided OSCR surface currents measured at (a) 1000 and (b) 1700 UTC 2 Aug 1996



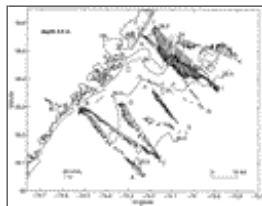
[Click on thumbnail for full-sized image.](#)

Fig. 8. Map 1: maximum vertical shear of the horizontal velocity normalized by the average vertical shear at the same location. Only contours 4 (dashed line) and 5 through 7 (solid lines) are shown



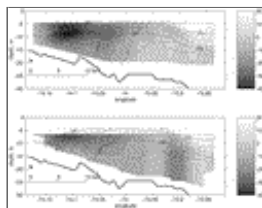
[Click on thumbnail for full-sized image.](#)

Fig. 9. Transects AB (top) and IJ (bottom) of map 1: vertical distribution of density (dashed lines) and Richardson number Ri (solid lines). The heavy line is the bottom. Contour intervals are 0.5 kg m^{-3} for density and 10 for Ri



[Click on thumbnail for full-sized image.](#)

Fig. 10. As in [Fig. 4a](#) but for map 2 at 4.5-m depth



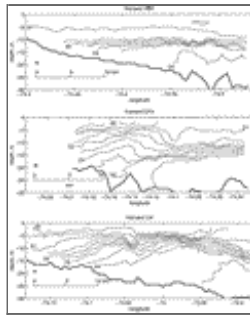
[Click on thumbnail for full-sized image.](#)

Fig. 11. Map 2 vertical transect JK: (a) detided alongshelf velocity component and (b) geostrophic alongshelf velocity relative to observed velocity at 6.5-m depth. Density (solid and dashed lines) is shown in both plots. Heavy line is bottom. Contour intervals are 5 cm s^{-1} for velocity and 0.5 kg m^{-3} for density



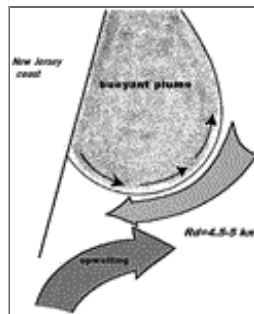
[Click on thumbnail for full-sized image.](#)

Fig. 12. As in [Fig. 4a](#) but for map 4 at 4.5-m depth



[Click on thumbnail for full-sized image.](#)

Fig. 13. Map 4 vertical distribution of the density along transects (a) AB, (b) EF, and (c) IJ. The heavy line is the bottom



[Click on thumbnail for full-sized image.](#)

Fig. 14. Schematic of the observed velocity field driven by buoyancy and wind forcing

Corresponding author address: Dr. Alexander E. Yankovsky, Oceanographic Center, Nova Southeastern University, 8000 North Ocean Drive, Dania Beach, FL 33004-3078.

E-mail: sasha@nova.edu

[top ▲](#)



© 2008 American Meteorological Society [Privacy Policy and Disclaimer](#)
Headquarters: 45 Beacon Street Boston, MA 02108-3693
DC Office: 1120 G Street, NW, Suite 800 Washington DC, 20005-3826
amsinfo@ametsoc.org Phone: 617-227-2425 Fax: 617-742-8718
[Allen Press, Inc.](#) assists in the online publication of AMS journals.